ACS APPLIED MATERIALS & INTERFACES

www.acsami.org

Research Article

Highly Conductive Sb–SnO_2 Nanocrystals Synthesized by Dual Nonthermal Plasmas

Qinyi Chen and Elijah Thimsen*

Cite This: *ACS Appl. Mater. Interfaces* 2020, 12, 25168–25177

Read Online

ACCESS | Metrics & More | Article Recommendations | Supporting Information

ABSTRACT: Nonthermal plasma synthesis of transparent conducting oxide nanocrystals can offer advantages, for example, ligand-free surfaces, over traditionally used colloidal synthesis methods. When it comes to multicomponent (doped) metal oxide nanocrystal synthesis, uniform distribution of different metal elements and suppressing surface segregation of secondary resistive phases have been concerns. Specifically, surface segregation of resistive secondary phases reduces the electrical conductivity of nanocrystal assemblies. In this work, we demonstrate a nonthermal dual-plasma synthesis method capable of forming Sb–SnO_2 (ATO) nanocrystals with a uniform composition distribution and apparently insignificant surface segregation of the dopant. A drastic increase in conductivity was observed in ATO thin films comprised of nanocrystals formed using a dual-plasma configuration compared to nanocrystals formed using a single-plasma configuration. The conductivity values of as-deposited porous films comprised of ATO nanocrystals, prepared using the dual-plasma approach, were on the order of 0.1 S cm^{-1}, which to our knowledge is the highest conductivity reported to-date for that type of high surface area material. Annealing the films comprised of ATO nanocrystals at 500 °C for 2 h in air increased the conductivity and improved ambient stability, without significantly affecting the crystallite size.

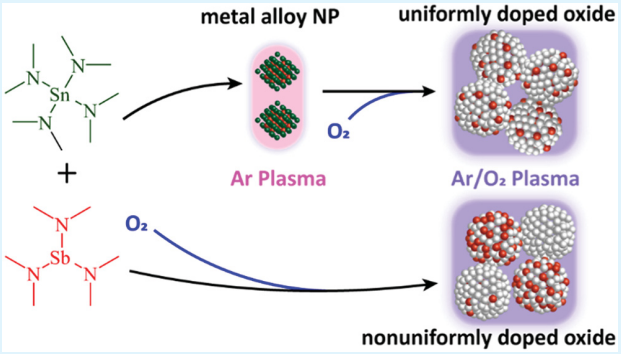

KEYWORDS: *non-thermal plasma, nanocrystal, antimony-doped tin oxide (ATO), doping, dual plasma, conductivity*

INTRODUCTION

Transparent conducting oxides (TCOs) find application in a wide variety of areas, ranging from top contacts in optoelectronic devices such as light-emitting diodes[1,2] and displays[3,4] to architectural glass[5−7] to electrochemical applications such as dimensionally stable anode materials.[8−10] For optoelectronic applications, thin films comprised of TCO nanocrystals have attracted attention because they can be deposited by high-throughput printing processes at lower cost when compared to conventional semiconductor processing methods.[11] For electrochemical applications, some TCO materials have attracted attention because they can be more chemically rugged when compared to high surface area conductive carbon supports, which typically have a network conductivity in the range from 10 to 100 S cm^{-1}.[12,13] Of the TCO materials, antimony tin oxide (ATO, Sb–SnO_2) is among the most chemically and thermally stable. In particular, ATO is stable under acidic conditions at highly oxidizing potentials that are often encountered in fuel cells used for automotive applications. Thus, ATO is a more stable support material for the oxygen reduction reaction when compared to carbon black.[14−20]

ATO nanocrystals can be synthesized by colloidal processing.[21−25] High-quality materials can be prepared by this route,[21,23] but there are some drawbacks to the solution phase. Notably, colloidal processing requires large amounts of solvent that is typically toxic in nature, which gives rise to environmental concerns. Beyond that, proper disposal of used solvents for colloidal synthesis and processing incurs additional expense. Furthermore, nanocrystals produced by colloidal routes typically have surface ligands to stabilize them in solution. After a film is deposited from colloidal nanocrystals, those ligands remain and can cause a significant impediment to charge transport and thereby decrease the conductivity of the assembly.[21,23] Nevertheless, dense films can be deposited from colloidal particles, nearing the random closed packed limit of approximately 60% relative density.[26] The highest reported conductivity values for ATO films comprised of nanocrystals are on the order of 10^{-2} S cm^{-1} in the as-deposited state and in the range 10 to 100 S cm^{-1} after annealing in air.[21]

Received: March 17, 2020
Accepted: May 12, 2020
Published: May 12, 2020

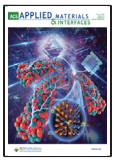

Gas-phase processing involving aerosols of SnO_2 particles provides a route to films comprised of nanocrystals that does not involve solvents or surface ligands. For example, combustion[27,28] and thermal plasma[29] have been used to make films comprised of SnO_2 nanocrystals. However, the materials prepared by the combustion route are heavily agglomerated and extremely resistive[28] and therefore of limited utility in optoelectronic and electrochemical applications. Nonthermal plasma synthesis, on the other hand, is capable of synthesizing highly conductive undoped TCO nanocrystals.[2,30−32] When compared to flame synthesis, which often results in hard aggregates, nanopowders and films collected from nonthermal plasma processing are typically softly agglomerated.[33] Agglomeration in the plasma is suppressed by unipolar negative charging of the nanocrystals by fast free electrons.[33] Other advantageous features of nonthermal plasma processing of semiconductor nanocrystals have been described elsewhere.[1,2,33] A major challenge facing the synthesis of doped nanocrystals by nonthermal plasma is surface segregation of the dopant.[1,34,35] If the dopant forms a resistive oxide at the surface, such as Al_2O_3 in the case of Al−ZnO[1] or Sb_2O_5 in the case of ATO, then the conductivity of the assembly suffers. In other words, there is a gap in knowledge of how to synthesize uniformly doped nanocrystals by nonthermal plasma that exhibit a high assembly conductivity.

In this work, we present a processing concept for how to synthesize multicomponent (e.g. doped) metal-oxide nanocrystals by nonthermal plasma with a uniform composition distribution and apparently without significant segregation of the dopant. The concept involves two sequential stages and is termed a dual-plasma process. The first stage causes the metal precursors to react and metal components to mix, without oxidation, to form alloy particles. Oxygen is then added to the stream, and in a second plasma, those alloy particles are oxidized to form metal oxide nanocrystals. The process concept, illustrated in Figure 1, is demonstrated using Sb−

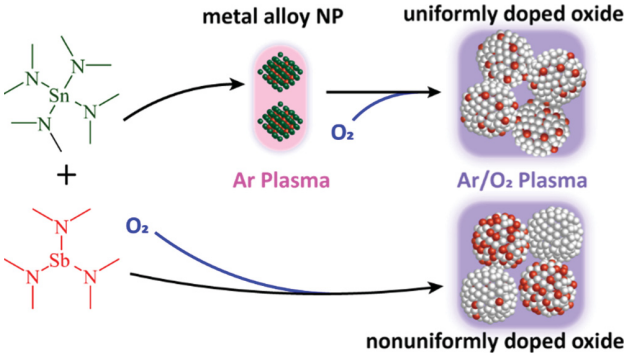

Figure 1. Processing concept. Synthesis of uniformly doped ATO nanocrystals is enabled by a dual-plasma approach.

SnO_2. The dual nonthermal plasma process can synthesize highly conductive, high surface area, and high porosity films comprised of ATO nanocrystals in a single step, and those unique material features enable application in electrochemical devices. Films comprised of nanocrystals synthesized by the dual-plasma approach have far superior conductivity to samples synthesized using a single plasma wherein metal precursors and oxygen are co-fed together. Furthermore, the conductivity of films comprised of ATO nanocrystals synthesized by the dual-plasma approach is on the order 0.1 S cm^{-1} in the as-deposited state, which is an order of magnitude greater than the highest performance reported in the colloidal literature and the highest conductivity ever reported for as-deposited thin films of this type. Furthermore, such high conductivity was achieved with films that have low relative density of approximately 30%. Annealing of the films at 500 °C in air increased conductivity into the range from 10 to 100 S cm^{-1} and improved ambient stability, without significant grain growth or change in relative density. Thus, assemblies comprised of these chemically robust ATO nanocrystals are competitive with high surface area carbon black electrodes. Similar network conductivity and specific surface area can be achieved using a more chemically robust material platform.

EXPERIMENTAL SECTION

Synthesis of ATO Nanocrystals. ATO nanocrystals were synthesized using a flow-through reactor similar to the one previously reported;[2] however, the system concept was modified by adding an additional discharge zone, thereby allowing the reactor to be operated in either a single- or dual-plasma configuration. A schematic of the reactor is presented in Figure 2. The discharge tube had inner and outer diameters of 13 and 19 mm, respectively. Two organometallic precursors were fed into the reactor via different temperature-controlled gas bubblers. The tin (Sn) precursor, tetrakis-(dimethylamido)tin (TDMASn, Strem, Newburyport MA), bubbler was maintained at a constant temperature of 55 °C. The vapor delivery lines were also heated to at least 55 °C to prevent condensation. The antimony (Sb) precursor, tris(dimethylamido)-antimony (TDMASb, Sigma-Aldrich, Saint Louis MO), was cooled using an ice-bath and maintained at a constant temperature of 0 °C. The total pressure in the TDMASb bubbler was controlled in the range from 20 to 160 Torr to produce nanoparticles with dopant fractions from 3 to 20% based on Sn. In a typical synthesis, the Sn and Sb vapor precursors were fed into the reactor using argon (Ar) as the carrier gas at a flow rate of 30 standard cubic centimeters per minute (sccm) for each. Flow rates were controlled using mass flow controllers (GE50A, MKS Instruments, Andover MA). The metal-organic precursor flows were combined with an additional dilution Ar flow of 270 sccm, and all three flows were introduced into the top inlet of the reactor. The diluted metal organic precursor flows were sent through a zone in which a first plasma could be ignited in the absence of oxygen, if a dual-plasma synthesis was being conducted. If a single-plasma synthesis was being conducted, then this first plasma was off. Downstream of the first plasma zone, pure oxygen (O_2) gas was introduced at a constant flow rate of 100 sccm, through the bottom inlet (Figure 2). Immediately downstream of the O_2 inlet, where both metalorganic precursors and O_2 were present, was a second zone in which a plasma could be ignited. For both single- and dual-plasma syntheses, this second plasma was on (i.e., it was the only plasma for single-plasma synthesis). The total pressure in the portion of the reactor where nanocrystal synthesis took place was 15 Torr. The electrodes used to generate the plasma were identical aluminum rings mounted on the outside of the fused silica tube. The rings were 10 mm thick and separated by a 15 mm gap. In both the first- and second-plasma zones, one ring was powered and the other was grounded. The two plasmas were generated using separate radio-frequency (RF, 13.56 MHz) power supplies (AG 0613, T&C Power Conversion) that were coupled to the electrodes through separate impedance matching networks. To prevent coupling between the first and second plasmas, the two plasma zones were spaced 70 mm apart. An RF power of 50 W was used to generate the first plasma, and the power applied to the second plasma was in the range from 80 to 100 W.

In a typical dual-plasma synthesis, Sn and Sb vapor precursors were fed into the first plasma to form metallic Sb−Sn alloy nanoparticles. These alloy nanoparticles followed the flow field of carrier gas and were introduced into second plasma together with O_2. Under typical synthesis conditions, the average residence time in the first plasma

https://dx.doi.org/10.1021/acsami.0c05039
ACS Appl. Mater. Interfaces 2020, 12, 25168−25177

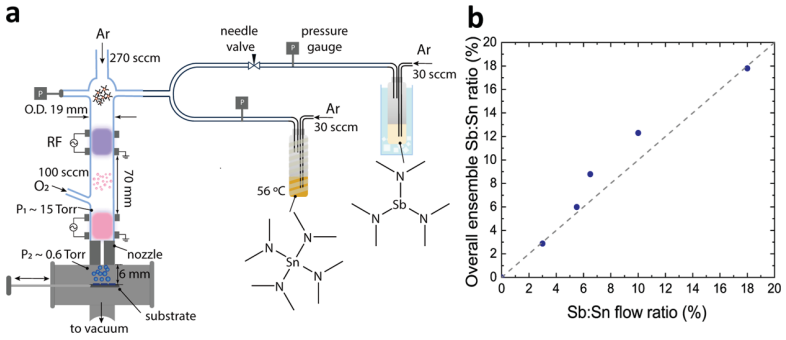

Figure 2. Experimental apparatus. (a) Schematic illustration of the ATO nanoparticle synthesis and deposition reactor. The ATO nanoparticles were synthesized from the dual plasma system and then deposited by inertial impaction. (b) Dependence of the Sb/Sn ratio (measured by XPS) on the nominal Sb/Sn flow ratio. Dashed line (grey) indicates a 1:1 dependence on the flow ratio. Because the measured composition was similar to the nominal value expected from the flow rates, the nominal values are used in the text.

was 6.3 ms, and the residence time in the second plasma was approximately 4.8 ms. ATO nanocrystals exited the second plasma as an aerosol. The aerosol was then passed through a custom-made nozzle. The geometry of the nozzle was 67 mm in length, with a slit area of 0.8 mm × 20 mm and the nozzle stand-off distance from the substrate holder of 6 mm. The ATO nanocrystals were accelerated to supersonic velocity by passing through the nozzle and exited as a particle beam.[36] The pressure ratio across the nozzle was 23, and the downstream pressure was approximately 0.66 Torr. The ATO nanocrystals were then deposited by inertial impaction onto various substrates (silicon wafer, glass, fused silica, or single crystal NaCl) that were placed in the path of the particle beam. The substrates were mounted onto a pushrod, which was moved back and forth during deposition to allow for the formation of thin films from the impacting nanocrystals. A typical deposition rate was 0.55 nm s^{-1}.

Post treatment annealing of ATO thin films was carried out using a laboratory-built system under flowing air. ATO thin films were placed into a tube furnace and then heated to 500 °C at a ramp rate of 2.5 °C min^{-1}. The films were held at 500 °C for a duration of 2 h. After annealing, the samples were cooled down to room temperature over approximately 3 h.

Transmission Electron Microscopy and Energy-Dispersive X-ray Spectroscopy. Samples used for transmission electron microscopy (TEM) and scanning TEM (STEM) were prepared by directly depositing ATO and antimony−tin (Sb−Sn) alloy nanoparticles onto carbon-coated copper grids (part number 01824, Ted Pella, Redding CA) via inertial impaction. The deposition time was 10, 20, and 60−90 s, respectively, for Sb−Sn alloy, ATO from single plasma, and ATO from dual plasmas. Nanoparticle characterization was performed on a JEOL JEM-2100F field-emission transmission electron microscope operating at an accelerating voltage of 200 kV that was equipped with an energy-dispersive X-ray spectrometer (EDS, XFlash Detector 5060, Bruker Nano GmbH, Berlin, Germany). Bright-field images were taken in TEM mode. Composition distributions were acquired by measuring EDS spectra from 102 spots of single-plasma sample and 85 spots of dual-plasma sample in STEM mode with a spot size of 1 nm. EDS spectra of Sn Kα (~26.3 keV) and Sb Kα (~25.0 keV) were acquired between the energy range from 0 to 40 keV, in a step size of 10 eV, with a 120 s integration, by focusing the beam on random spots on NCs.

X-ray Diffraction. X-ray diffraction (XRD) experiments were performed to determine the crystal structure of metallic Sb, metallic Sn, Sb−Sn alloy, and ATO samples deposited on silicon and glass substrates. Substrates were moved in a narrow range or held still under the nozzle for 6−30 min to achieve a sufficiently high areal mass density on the substrate. XRD patterns for the various samples were acquired on a D8 Advance diffractometer (Bruker, Billerica, MA) using a Cu radiation source (Cu Kα, λ = 1.541 Å). The XRD patterns were collected for 2θ values in the range 20−65°, with a step of 0.02° and a fixed counting time of 0.5 s per step. The crystallite size was calculated from the most intense SnO_2 (110) peak using the Scherrer equation, assuming spherical grains. For more precise measurement to determine lattice parameters, lanthanum hexaboride (LaB_6) was added to ATO samples as an internal standard, and the counting time was 4 s per step. LaB_6 (110) peaks were used as a reference to correct for slight alignment discrepancies between samples. The lattice parameters were determined using Rietveld refinement with the program Profex.

Ellipsometry. Film thickness and SnO_2 volume fraction were measured using an α-SE spectroscopic ellipsometer (J.A. Woollam, Lincoln NE) with an incident angle of 70°. The Bruggeman effective medium approximation was used to model the porous thin film and fit the spectra of samples in the wavelength range from 400 to 800 nm. The use of an effective medium approximation is justified by the fact that both the nanocrystals and pores in the film were much smaller than all wavelengths of the light that was used. The model consisted of three layers: silicon substrate, native oxide thickness of 1.6 nm, and sample film layer that was treated using the effective medium approximation. The film was assumed to be composed of SnO_2 and voids.[37]

Scanning Electron Microscopy. ATO films were deposited on silicon substrates and then cleaved using a diamond scribe to make a sharp edge. The cross sections were imaged edge-on. The scanning electron microscopy (SEM) images were obtained using a Thermo Fisher Quattro S ESEM operating at an accelerating voltage of 10 kV.

X-ray Photoelectron Spectroscopy. The elemental composition of ATO film samples was measured using X-ray photoelectron spectroscopy (XPS) on a Physical Electronics PHI 5000 VersaProbe II with monochromatic Al Kα line (1486.6 eV) illumination. The samples were cleaned by Ar^+ sputtering for 1 min at 2 keV. The quantification of the Sb/Sn ratio was performed using calibrated peak areas of Sn $3d_{3/2}$ and Sb $3d_{3/2}$.

Electrical Measurements. For electrical characterization, ATO films were deposited on SiO_2/Si substrates (300 nm SiO_2 on 100 Si) and press-bonded metallic indium served as contact pads. Room-temperature Hall effect measurements were carried out using an Ecopia HMS-5000, and samples had a van der Pauw electrode configuration. The magnetic field was constant 0.542 T.

Photospectroscopy. For ultraviolet−visible (UV−vis) transmission spectroscopy, ATO films were deposited onto fused silica substrates and measured under ambient condition using a spectrophotometer (Varian Cary 50 Bio). Fourier transform infrared (FT-IR) spectroscopy was measured using Nicolette Nexus 470 operating in transmission mode. Uncoated NaCl substrates were used for FT-IR spectroscopy. The spectra were baselined using the transmission spectrum of a blank NaCl substrate.

RESULTS AND DISCUSSION

Achieving uniform composition is one of the fundamental challenges in plasma synthesis of doped nanocrystals.

https://dx.doi.org/10.1021/acsami.0c05039
ACS Appl. Mater. Interfaces 2020, 12, 25168−25177

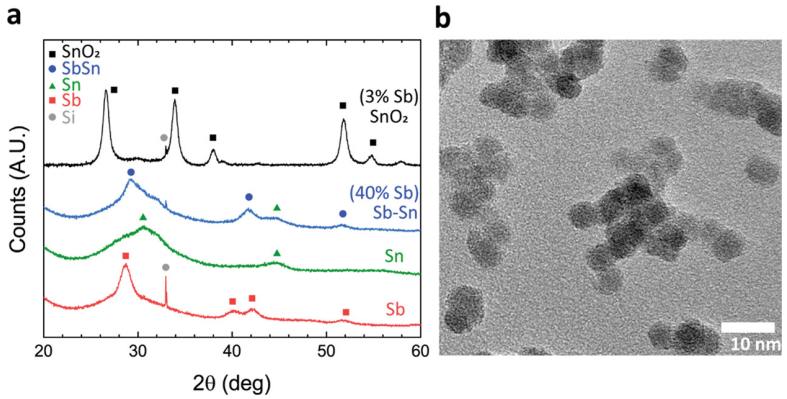

Figure 3. Thin film characterization. (a) XRD pattern of as-deposited tin dioxide (PDF 00-041-1445), $Sb_{0.5}Sn_{0.5}$ alloy (PDF 00-033-0118), metallic Sn (PDF 00-004-0672), and metallic Sb (PDF 00-005-0562). The metallic films were synthesized under Ar plasma. (b) Representative TEM micrographs of Sb−Sn alloy nanoparticles synthesized under Ar plasma.

Uniformity in this context has two meanings, and those meanings will be treated in sequence.

First, one must consider the population of nanocrystals. The overall ensemble stoichiometry can be controlled via the relative feed rates of the different precursors, which is evidenced in Figure 2b. However, at the single nanocrystal level, there is always a distribution in composition. The first meaning of uniformity is that each of the nanocrystals has similar overall composition, or in other words, that the composition distribution is narrow. A uniform composition distribution can be achieved by rapid mass exchange between the nanocrystals in the synthesis environment. Collisions between nanoparticles in a nonthermal plasma are suppressed by Coulombic repulsion, which is caused by unipolar negative charging.[33] Therefore, mass exchange through the vapor phase is more promising as a route to achieve rapid mixing and a uniform composition distribution. Our group has recently demonstrated that if metallic elemental nanoparticles are fed into a nonthermal plasma similar to the one used here, then those particles rapidly vaporize and mass is exchanged to create alloyed nanocrystals.[38] As one might expect, materials with a low surface binding energy more easily vaporize in this nonequilibrium environment than materials with high surface binding energy.[38−40] Thus, nanoparticles comprised of metallic elements are expected to mix more rapidly to achieve a uniform composition distribution when compared to refractory materials containing the same elements, such as the corresponding nitrides[39] and oxides.

Second, at a single nanocrystal level, the goal is to have the composition be uniformly distributed in the particle interior. This is a well-recognized challenge in the synthesis of doped nanocrystals.[41] In the case of nanocrystals comprised of doped TCOs, suppressing surface segregation is a primary challenge because the secondary phases are resistive.[1] If the mixed phase of the dopant and matrix is thermodynamically favorable, then at the single nanocrystal level, achieving a uniform composition is facilitated by having a large solid-state diffusion coefficient. Again from this perspective, it is advantageous to mix the elements in the metallic state before oxidation. To illustrate this idea, consider the solid-state diffusion coefficient of Sb in Sn compared to Sb in SnO_2. The diffusion coefficient of Sb in SnO_2 is 10^{-19} cm^2 s^{-1} at 560 °C,[42] which is 8 orders of magnitude smaller than the value of Sb in solid Sn metal, which is 10^{-11} cm^2 s^{-1} at 209 °C.[43] It is reasonable to consider these elevated temperatures because the plasma has the ability to heat nanoparticles to temperatures that can be hundreds of degrees higher than background gas temperature.[44−46] If the temperature of metallic nanoparticles is higher than their melting point, liquid metal solution (Sb−Sn) will be formed. The diffusion coefficient of Sb in liquid Sb−Sn metal solution is even higher, 10^{-5} cm^2 s^{-1} at 450 °C.[47] Consequently, if the goal is to synthesize nanocrystals with a spherically uniform dopant fraction in the interior, then there is a clear advantage to mixing the elements in a metallic state before oxidation, when compared to co-feeding both the metallic precursors and oxygen into a single discharge.

Taking the above considerations in mind, we pursued a dual-plasma strategy to synthesize Sb−SnO_2 nanocrystals with a uniform composition distribution that provided high electrical conductivity in the as-deposited state. The general idea is to feed the metal precursors together with argon gas into a first plasma, wherein the precursors decompose into the constituent metallic elements. In the first plasma, metallic particles easily vaporize, and mass exchange resulting from that vaporization creates alloyed Sb−Sn nanoparticles, similar to our previous results on GaSb.[38] These alloy particles can then be oxidized in a second plasma by adding O_2 to the aerosol after the first plasma. When compared to a single-plasma approach, which involves co-feeding the metal precursors and O_2 simultaneously, the sequential dual-plasma approach of metal alloy formation followed by oxidation to metal-oxide resulted in a much more uniform composition distribution and much higher electrical conductivity.

Metallic and metallic alloy nanoparticles were synthesized in the first plasma. Experiments were conducted in which TDMASn, TDMASb, and Ar were fed into the first plasma, while the oxygen flow, and second plasma, were off. The nanoparticles were collected on a silicon substrate by supersonic impact deposition and then characterized by XRD. If only Sn precursor was on, and no Sb precursor was used, then the XRD pattern was consistent with metallic tin (Figure 3a, tetragonal structure, space group $I4_1/amd$, JCPDS file card no. 04-0673). Similarly, if only Sb precursor was fed into the first plasma, then the nanoparticles collected on the substrate were metallic Sb (Figure 3a, tetradymite structure, space group $R\bar{3}m$, JCPDS file card no. 05-0562). For small mol fractions of Sb in Sn, there is little change in the crystal structure of the host Sn lattice and thus mixing would be

https://dx.doi.org/10.1021/acsami.0c05039
ACS Appl. Mater. Interfaces 2020, 12, 25168−25177

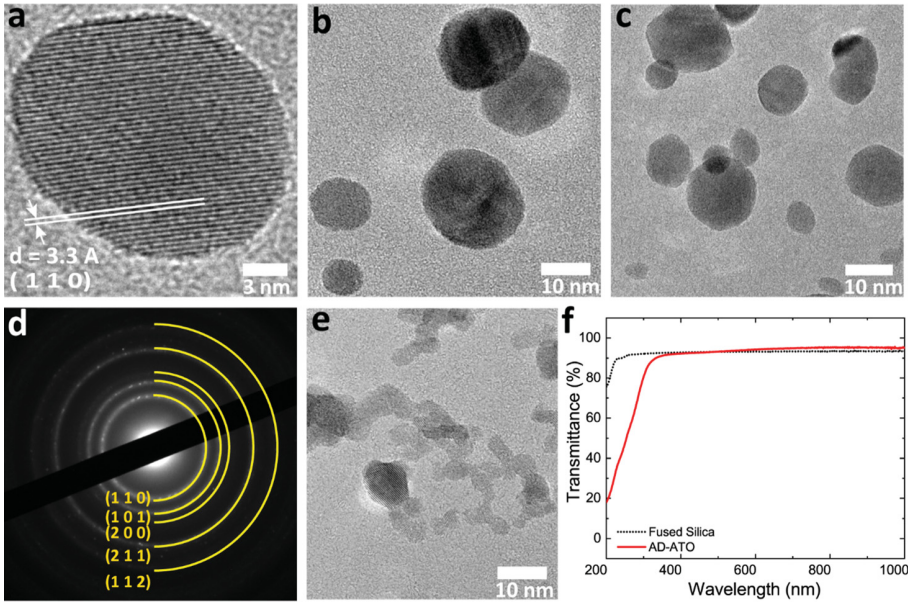

Figure 4. TEM analysis of ATO nanocrystals. Morphology of ATO nanoparticles with 3% Sb/Sn ratio. (a) TEM image of nanocrystals with a tetragonal crystal structure synthesized by dual plasmas. (b,c) Representative TEM micrographs of ATO nanocrystals synthesized by dual plasmas. (d) Selected area electron diffraction pattern of nanocrystals synthesized by single plasma. (e) Overview of the nanocrystals synthesized by single plasma. (f) UV−vis transmittance spectrum of a bare fused silica substrate (dashed) and as-deposited film comprised of ATO nanocrystals with 3% Sb/Sn of 170 nm thickness on fused silica substrate (solid).

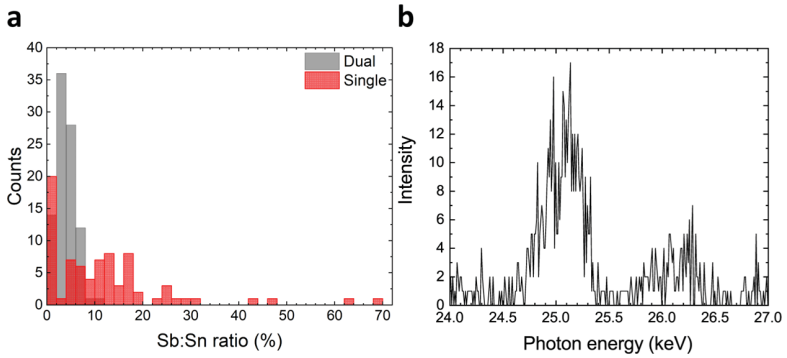

Figure 5. Composition uniformity. (a) Histogram of the Sb/Sn ratio measured from STEM−EDS on samples comprised of ATO nanocrystals having Sb/Sn of 18% with different plasma synthesis configurations: dual plasmas (grey) and single plasma (red). (b) Selected STEM−EDS spectrum of an ATO 18% nanocrystal synthesized by single plasma.

difficult to demonstrate by XRD. However, several line compounds exist on the Sb−Sn phase diagram,[48] which have unique diffraction patterns that are not linear superposition of the metallic elements. Thus, we performed an experiment at high Sb concentration, specifically a flow ratio of Sb/Sn that was 40%. At this overall composition, a physical mixture of the SbSn alloy and Sn metal is expected at equilibrium.[48] Indeed, the XRD pattern displayed a distinct peak at $2\theta = 29.2°$ that was not present in either the Sb or Sn diffraction patterns (Figure 3a), which is consistent with an Sb−Sn alloy (rhombohedral structure, space group $R\bar{3}m$, JCPDS file card no. 33-0118). There were also features in the pattern consistent with the Sn metal, as expected given the equilibrium phase mixture described by the phase diagram. Moreover, the material was composed of nanocrystals (Figure 3b). The conclusion of this experiment is that the first plasma does, indeed, promote mixing of the metallic elements to form metallic alloy nanoparticles in the first plasma of the dual-plasma process. The same behavior is also expected for smaller Sb flow fractions that would be more relevant for Sb−SnO_2, in the range from 1 to 10%.[21,23,49−51]

If oxygen was added to the aerosol eluting from the first plasma, then metal-oxide nanocrystals were synthesized in the second plasma of the sequential dual-plasma process. An XRD pattern acquired from a sample of nanocrystals comprised of ATO nanocrystals with 3% Sb/Sn ratio is presented in Figure 3a, which clearly demonstrates that the material was crystalline tetragonal, cassiterite SnO_2 (PDF 00-041-1445). An example UV−vis transmission spectrum of a film comprised of Sb−SnO_2 (3% Sb) nanocrystals, 170 nm in thickness deposited on a fused silica substrate, is presented in Figure 4f. The film displayed very high transmittance, 90% or greater, over the entire visible wavelength range, which further confirms that the metal particles had been oxidized. As an aside, similar experiments conducted without the second plasma and without oxygen produced films with a metallic appearance

https://dx.doi.org/10.1021/acsami.0c05039
ACS Appl. Mater. Interfaces 2020, 12, 25168−25177

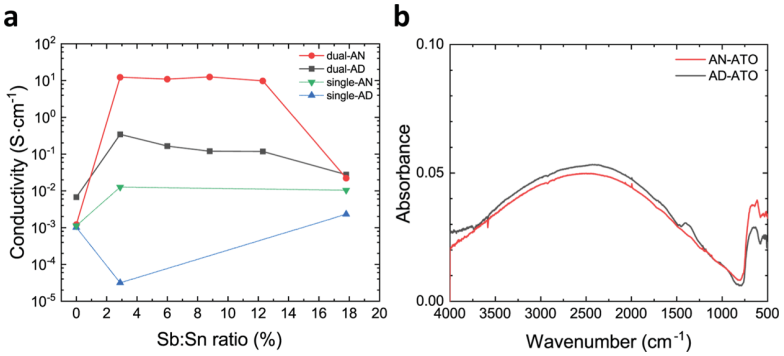

Figure 6. Longitudinal and local conductivity. (a) Conductivity of films comprised of ATO nanocrystals as a function of composition. The various samples were synthesized by single plasma and dual plasmas, with different post processing: as-deposited (AD) and annealed at 500 °C in air for 2 h (AN). (b) FT-IR absorption spectra of films comprised of ATO nanocrystals (3% Sb) deposited on NaCl substrates before (AD) and after (AN) annealing at the same conditions as (a).

(data not shown). Bright field TEM images of the ATO nanocrystals produced by the dual-plasma approach are presented in Figure 4a–c. The mean diameter was 12 nm, and the geometric standard deviation of the log normal distribution was 1.7. The high-resolution TEM image in Figure 4a demonstrated that the nanocrystals produced by the dual-plasma approach had a single crystallographic orientation. The composition distribution was characterized using STEM–EDS by acquiring spectra from 85 points and using the Kα lines of Sn and Sb. The K lines are less intense than the L lines, but extensive overlap between Sb and Sn L lines made deconvolution prohibitively difficult. To compensate for weak emission from K lines, samples were prepared at a nominal Sb/Sn ratio of 18% to increase the intensity of the Sb Kα line. A possible reason for the deviation of the dual plasma Sb/Sn ratio from the nominal value is that a small amount of Sb^{5+} dopants in the SnO_2 structure was ejected as damage was done to the metal-oxide material during the long dwell times used for composition measurements by STEM.[52] The composition distribution of the ATO nanocrystals produced by the dual-plasma approach was relatively narrow (Figure 5a), meaning most particles had a very similar Sb/Sn ratio, as expected given the rapid mixing in the first plasma prior to oxidation. Furthermore, there was a systematic distortion in the SnO_2 lattice parameters with increasing Sb content, as characterized by XRD (Figures S1, S2 and Table S1).

In comparison to the material produced by the dual-plasma approach, the nanoparticles produced by the single-plasma approach, in which organometallic precursors and O_2 were simultaneously fed into one plasma, were smaller in size and more heterogeneous in composition. TEM images of ATO nanocrystals produced at the same flow conditions as Figure 4a–c, but with single-plasma instead of dual-plasmas, are presented in Figure 4e. The ATO particles, produced by single-plasma, were mostly crystalline SnO_2 (Figure 4d), with a mean particle diameter of 3.7 nm and a geometric standard deviation of 1.3. Although there was a narrower size distribution for the single-plasma nanocrystals, the composition distribution was extremely wide (Figure 5a). Indeed, despite the ensemble Sb/Sn ratio of 18%, some of the particles had more antimony than tin. In comparison to the dual-plasma approach, the single-plasma approach is clearly more likely to result in resistive secondary phases, that is, metal-oxides that are rich in Sb. The wide composition distribution in the case of single-plasma not only introduces resistive secondary phases but it also starves some SnO_2 particles of Sb dopants that are needed to increase conductivity. The expectation, therefore, is that the dual-plasma approach will produce much more conductive films comprised of ATO nanocrystals than the single-plasma approach.

The electrical conductivity of films comprised of ATO nanocrystals prepared using the dual-plasma approach was at least an order of magnitude higher than films prepared using the single-plasma approach, for Sb-dopant fractions of relevance to TCO applications. Conductivity measurements for both as-deposited films and films post-annealed in air at 500 °C for 2 h and both dual- and single-plasma, are presented in Figure 6a as a function of the Sb/Sn ratio. For thin films made using the dual-plasma configuration, the conductivity of intrinsic SnO_2 was 6.7×10^{-3} S cm^{-1}. The conductivity significantly increased with Sb doping and displayed a maximum of 0.34 S cm^{-1} at 3% Sb, a 50-fold increase compared to the pure SnO_2 thin film. As the Sb content was increased beyond 9%, a gradual decrease in the conductivity was observed, corresponding to a decrease in carrier concentration and mobility. At higher Sb content, increased disorder raises the activation energy of the donor, resulting in a decrease of carrier concentration.[53,54] Furthermore, carrier mobility is deteriorated by scattering of charge carriers in heavily doped samples.[54,55] In comparison, ATO films made using the single-plasma configuration exhibited very low conductivities with a maximum value of 3.1×10^{-5} S cm^{-1} at a Sb doping content of 3% in the as-deposited state. In other words, the most conductive dual-plasma films in the as-deposited state had approximately 100 times higher conductivity than the most conductive single-plasma films in the as-deposited state. For the single-plasma synthesis, the nanocrystals were smaller in size compared to dual-plasma, and the films were more porous, both of which tend to decrease the overall conductivity of the network through purely structural effects.[30] The conductivity decreases as a power law with decreasing film density (see Supporting Information). However, even after accounting for the effects of lower film density and smaller nanocrystal size, the conductivity of films comprised of nanocrystals synthesized by single-plasma was unexpectedly low when compared to dual-plasmas (see Supporting Information).

To our knowledge, the conductivity of 0.34 S cm^{-1} for the as-deposited 3% Sb ATO film by dual plasmas is the highest reported conductivity of a film comprised of ATO nanocrystals

https://dx.doi.org/10.1021/acsami.0c05039
ACS Appl. Mater. Interfaces 2020, 12, 25168–25177

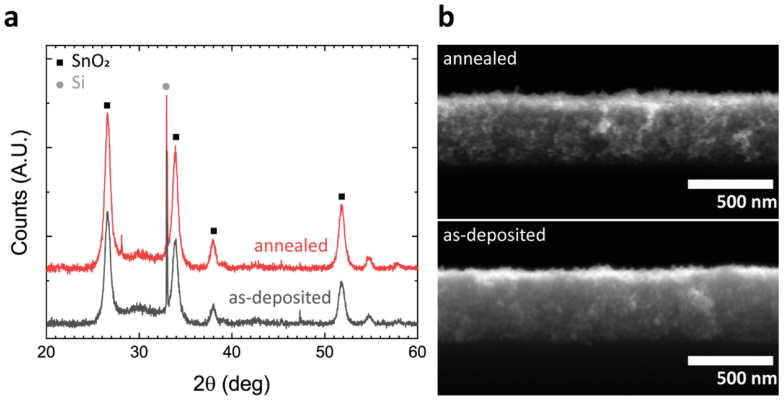

Figure 7. Annealing and structural changes. (a) XRD patterns of ATO nanocrystals synthesized at nominally identical conditions by dual plasma with different post processing: as-deposited (grey) and annealed at 500 °C for 2 h in air (red). The grain sizes determined by peak broadening using the Scherrer equation were 10.8 and 11.2 nm before and after annealing, respectively. (b) Cross-sectional SEM images of films comprised of ATO nanocrystals on silicon substrates processed by the same methods as panel (a).

without any thermal post-treatments. For comparison, the highest conductivity that has been previously reported was 6.8 × 10^{-2} S cm^{-1}, measured from pellets of as-prepared ATO nanoparticles synthesized using colloidal methods.[21] The higher conductivity of thin films comprised of ATO nanocrystals formed by the dual-plasma configuration reported in this work is consistent with the idea that enhanced electron transport can be achieved by using ligand-free nanocrystals.

Annealing at 500 °C for 2 h in air increased the conductivity, for films prepared by both dual- and single-plasma approaches. However, the dramatically higher conductivity for the dual-plasma preparation remained, even after annealing (Figure 6a). Take materials with 3% Sb for example. After annealing, the dual-plasma conductivity increased from 0.34 to 12 S cm^{-1}, while the single-plasma conductivity increased from 3.1 × 10^{-5} to only 1.3 × 10^{-2} S cm^{-1} (Figure 6a). A conductivity of 12 S cm^{-1} is technologically relevant for applications in which the electrode is required to be porous and to have a high specific surface area. Intrigued by the increase of conductivity with annealing in the dual-plasma case, we decided to investigate the changes in the material structure and properties that were caused by annealing.

Experiments were performed to characterize how the crystallite size and porosity of the film changed as a result of annealing for 3% Sb samples prepared by the dual-plasma approach. Crystallite size was determined by XRD peak broadening using the Scherrer equation (Figure 7a). Interestingly, the crystallite size was approximately the same before (10.8 nm) and after (11.2 nm) annealing. That result suggests that very little, if any, grain growth occurred. To verify that conclusion, we performed spectroscopic ellipsometry on the films before and after annealing and extracted the void fraction by modeling the ATO layer using an effective medium approximation. As expected, the relative density (i.e., SnO_2 volume fraction) was the same, within the experimental margin of error, before (28%) and after (30%) annealing. The conclusion of negligible change in solid volume fraction was also verified by SEM (Figure 7b). Thus, there were apparently no changes in either the nanocrystal size, or the conducting phase volume fraction, which are two key parameters that influence the conductivity of a nanocrystal network.[30] The remaining parameters that determine the conductivity are (1) the local majority carrier mobility, (2) the local majority carrier concentration, and (3) the inter-particle contact area. Because the nanocrystals produced by dual plasmas are already single crystals before annealing (Figure 4a), the local majority carrier mobility is not expected to change. Thus, experiments were performed to assess if the local majority carrier concentration changed as a result of annealing, for example, via dopant activation.

The majority carrier concentration was measured by FT-IR absorption spectroscopy and Hall effect measurements. The local majority carrier concentration can be found by fitting a Drude model to the FT-IR absorbance spectrum (Figure S3a,b, Supporting Information).[2] Samples were deposited on NaCl substrates, and the FT-IR absorbance spectrum was measured before and after annealing. The resulting plasmon peak was fit using a Drude model to extract the local majority carrier concentration and local majority carrier mobility (Figure 6b). The results of the fit are presented in Table 1. As expected, the local mobility did not change significantly as a result of annealing. Interestingly, also the local majority carrier concentration did not change as a result of annealing. Furthermore, the majority carrier concentration, measured by Hall effect after annealing, was very similar to the value extracted from the fit of the FT-IR absorbance spectrum, strengthening the conclusion (note: as-deposited films were too resistive to reliably perform Hall effect measurements). Therefore, annealing at 500 °C for 2 h in air apparently had no effect on the local electronic properties, and the increase in conductivity from 0.34 to 12 S cm^{-1} remains to be explained.

Table 1. Comparison of the Carrier Concentration and Mobility of as-Deposited and Annealed Films Comprised of ATO Nanocrystals with 3% Sb/Sn from Hall Effect and FT-IR Absorption Measurements

	as-deposited (AD)	annealed (AN)
longitudinal conductivity (S/cm)	0.3	12.4
Hall coefficient (cm^3/C)		−8.3 × 10^{-2}
Hall carrier concentration (cm^{-3})		−7.4 × 10^{19}
longitudinal mobility (cm^2 V^{-1} s^{-1})		1.0
local carrier concentration magnitude (cm^{-3})	7.1 × 10^{19}	7.7 × 10^{19}
local mobility (cm^2 V^{-1} s^{-1})	8	7

https://dx.doi.org/10.1021/acsami.0c05039
ACS Appl. Mater. Interfaces 2020, 12, 25168−25177

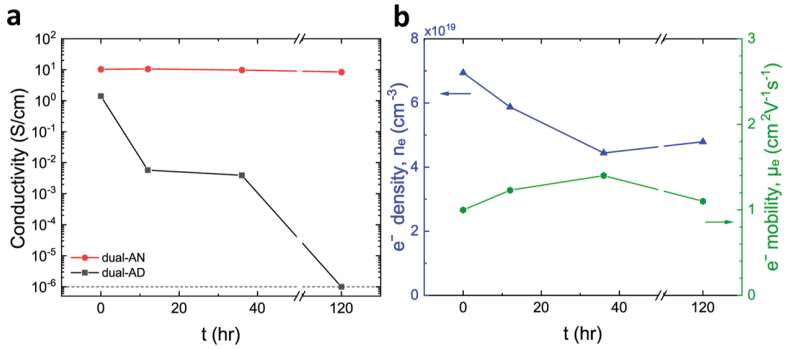

Figure 8. Conductivity as a function of time in ambient. (a) Conductivity of 3% Sb ATO samples with different post processing: as-deposited (AD, grey) and annealed at 500 °C for 2 h in air (AN, red) and different ambient storage time ranging from 0 to 120 h. Dashed line represents the lower limit of detection. (b) Electron density (blue triangle) and electron mobility (green hexagon) of annealed identical 3% Sb ATO samples stored in ambient with time up to 120 h.

By the process of elimination, the conductivity must be increasing as a result of increasing inter-particle contact area during annealing. In other words, annealing increases the strength of the contacts between particles in the network, which increases the network conductivity. This conclusion would suggest that the annealed nanocrystal networks would be more stable in the ambient compared to as-deposited samples. To test this hypothesis, we prepared a series of nominally identical films comprised of 3% Sb ATO nanocrystals and measured their conductivity as a function of time in the ambient. The annealed samples exhibited excellent ambient stability (Figure 8); however, the conductivity of the as-deposited samples decayed with increasing time.

CONCLUSIONS

In this work, a processing concept of using dual plasmas was presented as a means of synthesizing Sb−SnO_2 nanocrystals with uniform composition distribution and high electrical conductivity in the as-deposited state. Well-mixed metallic Sb−Sn alloy nanoparticles were synthesized in the first plasma from a mixture of metalorganic precursors. The metallic nanoparticles were then oxidized to Sb−SnO_2 nanocrystals in the second plasma after adding a feed of O_2. Taking advantage of mixing Sn and Sb elements in a metallic state, the dual-plasma process enabled a uniform distribution of the dopant element (Sb) and overcame the challenge of surface segregation of resistive phases. At a dopant ratio of 3% Sb/Sn, films comprised of ATO nanocrystals displayed a conductivity on the order of 0.1 S cm^{-1} with low relative film density of approximately 30%, which is the highest conductivity reported in the as-deposited state for materials of this type. It was also found that annealing of the films greatly increased conductivity and highly improved ambient stability. The work may expand the possibility for multicomponent metal-oxide nanocrystal synthesis through nonthermal plasma.

ASSOCIATED CONTENT

Supporting Information

The Supporting Information is available free of charge at https://pubs.acs.org/doi/10.1021/acsami.0c05039.

Diffraction patterns of as-deposited ATO samples with a Sb content up to 6%, Rietveld refinements on diffraction patterns of ATO samples with Sb up to 6%, refined values of lattice parameters of ATO samples with Sb up to 6%, model describing the dependency of film conductivity of film structural parameters, conductivity comparison of 3% Sb ATO film from single and dual plasma, and FT-IR absorption spectra of films comprised of ATO nanocrystals with 3% Sb/Sn both as-deposited and after annealing (PDF)

AUTHOR INFORMATION

Corresponding Author

Elijah Thimsen − *Institute of Materials Science and Engineering and Department of Energy, Environmental and Chemical Engineering, Washington University in Saint Louis, Saint Louis, Missouri 63130, United States;* orcid.org/0000-0002-7619-0926; Email: elijah.thimsen@wustl.edu

Author

Qinyi Chen − *Institute of Materials Science and Engineering, Washington University in Saint Louis, Saint Louis, Missouri 63130, United States*

Complete contact information is available at: https://pubs.acs.org/10.1021/acsami.0c05039

Author Contributions

The manuscript was written through contributions of all authors. All authors have given approval to the final version of the manuscript.

Notes

The authors declare no competing financial interest.

ACKNOWLEDGMENTS

Q.C. and E.T. acknowledge financial support from the National Science Foundation through Grant PHY-1702334 and the Army Research Office MURI Grant W911NF-18-1-0240. This work was performed in part at the Institute of Materials Science and Engineering and at the Nano Research Facility at Washington University in Saint Louis. Q.C. thanks Necip B. Uner for help measuring UV-vis spectra, and Trey Oldham for support on digital photography and participation of editing during the preparation of the manuscript.

REFERENCES

(1) Greenberg, B. L.; Ganguly, S.; Held, J. T.; Kramer, N. J.; Mkhoyan, K. A.; Aydil, E. S.; Kortshagen, U. R. Nonequilibrium-Plasma-Synthesized ZnO Nanocrystals with Plasmon Resonance Tunable Via Al Doping and Quantum Confinement. *Nano Lett.* **2015**, *15*, 8162−8169.

(2) Thimsen, E.; Johnson, M.; Zhang, X.; Wagner, A. J.; Mkhoyan, K. A.; Kortshagen, U. R.; Aydil, E. S. High Electron Mobility in Thin Films Formed Via Supersonic Impact Deposition of Nanocrystals Synthesized in Nonthermal Plasmas. *Nat. Commun.* **2014**, *5*, 5822.
(3) Katayama, M. TFT-LCD technology. *Thin Solid Films* **1999**, *341*, 140−147.
(4) Betz, U.; Kharrazi Olsson, M.; Marthy, J.; Escolá, M. F.; Atamny, F. Thin Films Engineering of Indium Tin Oxide: Large Area Flat Panel Displays Application. *Surf. Coat. Technol.* **2006**, *200*, 5751−5759.
(5) Kim, S.-H.; Yoko, T. Nonlinear Optical Properties of TeO_2-Based Glasses: MO_x-TeO_2 (M= Sc, Ti, V, Nb, Mo, Ta, and W) Binary Glasses. *J. Am. Ceram. Soc.* **1995**, *78*, 1061−1065.
(6) Lines, M. E. Oxide Glasses for Fast Photonic Switching: A Comparative Study. *J. Appl. Phys.* **1991**, *69*, 6876−6884.
(7) Llordés, A.; Garcia, G.; Gazquez, J.; Milliron, D. J. Tunable near-Infrared and Visible-Light Transmittance in Nanocrystal-in-Glass Composites. *Nature* **2013**, *500*, 323−326.
(8) Wang, Y.; Djerdj, I.; Smarsly, B.; Antonietti, M. Antimony-Doped SnO_2 Nanopowders with High Crystallinity for Lithium-Ion Battery Electrode. *Chem. Mater.* **2009**, *21*, 3202−3209.
(9) Binninger, T.; Mohamed, R.; Patru, A.; Waltar, K.; Gericke, E.; Tuaev, X.; Fabbri, E.; Levecque, P.; Hoell, A.; Schmidt, T. J. Stabilization of Pt Nanoparticles Due to Electrochemical Transistor Switching of Oxide Support Conductivity. *Chem. Mater.* **2017**, *29*, 2831−2843.
(10) Huang, S.-Y.; Ganesan, P.; Park, S.; Popov, B. N. Development of a Titanium Dioxide-Supported Platinum Catalyst with Ultrahigh Stability for Polymer Electrolyte Membrane Fuel Cell Applications. *J. Am. Chem. Soc.* **2009**, *131*, 13898−13899.
(11) Stadler, A. Transparent Conducting Oxides-An Up-To-Date Overview. *Materials* **2012**, *5*, 661−683.
(12) Subban, C. V.; Zhou, Q.; Hu, A.; Moylan, T. E.; Wagner, F. T.; DiSalvo, F. J. Sol−Gel Synthesis, Electrochemical Characterization, and Stability Testing of $Ti_{0.7}W_{0.3}O_2$ Nanoparticles for Catalyst Support Applications in Proton-Exchange Membrane Fuel Cells. *J. Am. Chem. Soc.* **2010**, *132*, 17531−17536.
(13) Parrondo, J.; Han, T.; Niangar, E.; Wang, C.; Dale, N.; Adjemian, K.; Ramani, V. Platinum supported on titanium-ruthenium oxide is a remarkably stable electrocatayst for hydrogen fuel cell vehicles. *Proc. Natl. Acad. Sci. U.S.A.* **2014**, *111*, 45−50.
(14) Zhang, P.; Huang, S.-Y.; Popov, B. N. Mesoporous Tin Oxide as an Oxidation-Resistant Catalyst Support for Proton Exchange Membrane Fuel Cells. *J. Electrochem. Soc.* **2010**, *157*, B1163−B1172.
(15) Takasaki, F.; Matsuie, S.; Takabatake, Y.; Noda, Z.; Hayashi, A.; Shiratori, Y.; Ito, K.; Sasaki, K. Carbon-Free Pt Electrocatalysts Supported on SnO_2 for Polymer Electrolyte Fuel Cells: Electrocatalytic Activity and Durability. *J. Electrochem. Soc.* **2011**, *158*, B1270−B1275.
(16) Masao, A.; Noda, S.; Takasaki, F.; Ito, K.; Sasaki, K. Carbon-Free Pt Electrocatalysts Supported on SnO_2 for Polymer Electrolyte Fuel Cells. *Electrochem. Solid-State Lett.* **2009**, *12*, B119−B122.
(17) Yin, M.; Xu, J.; Li, Q.; Jensen, J. O.; Huang, Y.; Cleemann, L. N.; Bjerrum, N. J.; Xing, W. Highly Active and Stable Pt Electrocatalysts Promoted by Antimony-Doped SnO_2 Supports for Oxygen Reduction Reactions. *Appl. Catal., B* **2014**, *144*, 112−120.
(18) Senoo, Y.; Taniguchi, K.; Kakinuma, K.; Uchida, M.; Uchida, H.; Deki, S.; Watanabe, M. Cathodic Performance and High Potential Durability of Ta-$SnO_{2-\delta}$-supported Pt Catalysts for Pefc Cathodes. *Electrochem. Commun.* **2015**, *51*, 37−40.
(19) Fabbri, E.; Rabis, A.; Kötz, R.; Schmidt, T. J. Pt Nanoparticles Supported on Sb-Doped SnO_2 Porous Structures: Developments and Issues. *Phys. Chem. Chem. Phys.* **2014**, *16*, 13672−13681.
(20) Dou, M.; Hou, M.; Liang, D.; Lu, W.; Shao, Z.; Yi, B. SnO_2 Nanocluster Supported Pt Catalyst with High Stability for Proton Exchange Membrane Fuel Cells. *Electrochim. Acta* **2013**, *92*, 468−473.
(21) Peters, K.; Zeller, P.; Stefanic, G.; Skoromets, V.; Němec, H.; Kužel, P.; Fattakhova-Rohlfing, D. Water-Dispersible Small Monodisperse Electrically Conducting Antimony Doped Tin Oxide Nanoparticles. *Chem. Mater.* **2015**, *27*, 1090−1099.
(22) Luo, L.; Bozyigit, D.; Wood, V.; Niederberger, M. High-Quality Transparent Electrodes Spin-Cast from Preformed Antimony-Doped Tin Oxide Nanocrystals for Thin Film Optoelectronics. *Chem. Mater.* **2013**, *25*, 4901−4907.
(23) Müller, V.; Rasp, M.; Štefanić, G.; Ba, J.; Günther, S.; Rathousky, J.; Niederberger, M.; Fattakhova-Rohlfing, D. Highly Conducting Nanosized Monodispersed Antimony-Doped Tin Oxide Particles Synthesized Via Nonaqueous Sol−Gel Procedure. *Chem. Mater.* **2009**, *21*, 5229−5236.
(24) Nütz, T.; Felde, U. z.; Haase, M. Wet-Chemical Synthesis of Doped Nanoparticles: Blue-Colored Colloids of N-Doped SnO_2: Sb. *J. Chem. Phys.* **1999**, *110*, 12142−12150.
(25) Conti, T. G.; Chiquito, A. J.; Da Silva, R. O.; Longo, E.; Leite, E. R. Electrical Properties of Highly Conducting SnO_2: Sb Nanocrystals Synthesized Using a Nonaqueous Sol−Gel Method. *J. Am. Ceram. Soc.* **2010**, *93*, 3862−3866.
(26) Finney, J. L.; Bernal John, D. Random Packings and the Structure of Simple Liquids. I. The Geometry of Random Close Packing. *Proc. Roy. Soc. Lond. Math. Phys. Sci.* **1970**, *319*, 479−493.
(27) Zhang, J.; Gao, L. Antimony-Doped Tin Oxide Nanocrystallites Prepared by a Combustion Process. *Mater. Lett.* **2004**, *58*, 2730−2734.
(28) Zheng, M.; Wang, B. One-Step Synthesis of Antimony-Doped Tin Dioxide Nanocrystallites and Their Property. *Trans. Nonferrous Met. Soc. China* **2009**, *19*, 404−409.
(29) Jung, D.-W.; Park, D.-W. Synthesis of Nano-Sized Antimony-Doped Tin Oxide (ATO) Particles Using a Dc Arc Plasma Jet. *Appl. Surf. Sci.* **2009**, *255*, 5409−5413.
(30) Lanigan, D.; Thimsen, E. Contact Radius and the Insulator-Metal Transition in Films Comprised of Touching Semiconductor Nanocrystals. *ACS Nano* **2016**, *10*, 6744−6752.
(31) Ephraim, J.; Lanigan, D.; Staller, C.; Milliron, D. J.; Thimsen, E. Transparent Conductive Oxide Nanocrystals Coated with Insulators by Atomic Layer Deposition. *Chem. Mater.* **2016**, *28*, 5549−5553.
(32) Chen, Q.; Guest, J. R.; Thimsen, E. Visualizing Current Flow at the Mesoscale in Disordered Assemblies of Touching Semiconductor Nanocrystals. *J. Phys. Chem. C* **2017**, *121*, 15619−15629.
(33) Kortshagen, U. Nonthermal Plasma Synthesis of Nanocrystals: Fundamentals, Applications, and Future Research Needs. *Plasma Chem. Plasma Process.* **2016**, *36*, 73−84.
(34) Hunter, K. I.; Bedford, N.; Schramke, K.; Kortshagen, U. R. Probing Dopant Locations in Silicon Nanocrystals Via High Energy X-Ray Diffraction and Reverse Monte Carlo Simulation. *Nano Lett.* **2019**, *20*, 852−859.
(35) Pi, X. D.; Gresback, R.; Liptak, R. W.; Campbell, S. A.; Kortshagen, U. Doping Efficiency, Dopant Location, and Oxidation of Si Nanocrystals. *Appl. Phys. Lett.* **2008**, *92*, 123102.
(36) Holman, Z. C.; Kortshagen, U. R. A Flexible Method for Depositing Dense Nanocrystal Thin Films: Impaction of Germanium Nanocrystals. *Nanotechnology* **2010**, *21*, 335302.
(37) Fujiwara, H.; Collins, R. W. *Spectroscopic Ellipsometry for Photovoltaics*; Springer, 2018.
(38) Uner, N. B.; Thimsen, E. Phase Mixing in Gasb Nanocrystals Synthesized by Nonequilibrium Plasma Aerotaxy. *Plasma Processes Polym.* **2020**, *17*, 1900233.
(39) Uner, N. B.; Thimsen, E. Nonequilibrium Plasma Aerotaxy of Size Controlled Gan Nanocrystals. *J. Phys. D: Appl. Phys.* **2019**, *53*, 095201.
(40) Uner, N. B.; Thimsen, E. In-Flight Size Focusing of Aerosols by a Low Temperature Plasma. *J. Phys. Chem. C* **2017**, *121*, 12936−12944.
(41) Norris, D. J.; Efros, A. L.; Erwin, S. C. Doped Nanocrystals. *Science* **2008**, *319*, 1776−1779.
(42) Dobler, D.; Oswald, S.; Werner, J.; Arabczyk, W.; Behr, G.; Wetzig, K. X-Ray Photoelectron Spectroscopy Investigation of Segregation Processes at Sb and in Doped SnO_2. *Chem. Phys.* **2003**, *286*, 375−383.

https://dx.doi.org/10.1021/acsami.0c05039
ACS Appl. Mater. Interfaces 2020, 12, 25168−25177

(43) Packwood, R. H.; Smith, R. W. The Diffusion of Antimony in Tin at Elevated Temperatures. *Scr. Metall.* **1970**, *4*, 947−951.
(44) Mangolini, L.; Thimsen, E.; Kortshagen, U. High-Yield Plasma Synthesis of Luminescent Silicon Nanocrystals. *Nano Lett.* **2005**, *5*, 655−659.
(45) Mangolini, L.; Kortshagen, U. Selective Nanoparticle Heating: Another Form of Nonequilibrium in Dusty Plasmas. *Phys. Rev. E: Stat., Nonlinear, Soft Matter Phys.* **2009**, *79*, 026405.
(46) Uner, N. B.; Thimsen, E. Low Temperature Plasma as a Means to Transform Nanoparticle Atomic Structure. *Plasma Sources Sci. Technol.* **2018**, *27*, 074005.
(47) Pasternak, A. D.; Olander, D. R. Diffusion in Liquid Metals. *AIChE J.* **1967**, *13*, 1052−1057.
(48) Okamoto, H. Sb-Sn (Antimony-Tin). *J. Phase Equilib. Diffus.* **2012**, *33*, 347.
(49) Ponja, S. D.; Williamson, B. A. D.; Sathasivam, S.; Scanlon, D. O.; Parkin, I. P.; Carmalt, C. J. Enhanced Electrical Properties of Antimony Doped Tin Oxide Thin Films Deposited Via Aerosol Assisted Chemical Vapour Deposition. *J. Mater. Chem. C* **2018**, *6*, 7257−7266.
(50) Terrier, C.; Chatelon, J. P.; Roger, J. A. Electrical and Optical Properties of Sb: SnO_2 Thin Films Obtained by the Sol-Gel Method. *Thin Solid Films* **1997**, *295*, 95−100.
(51) Terrier, C.; Chatelon, J. P.; Berjoan, R.; Roger, J. A. Sb-Doped SnO_2 Transparent Conducting Oxide from the Sol-Gel Dip-Coating Technique. *Thin Solid Films* **1995**, *263*, 37−41.
(52) Jiang, N. Electron Beam Damage in Oxides: A Review. *Rep. Prog. Phys.* **2015**, *79*, 016501.
(53) Rohatgi, A.; Viverito, T. R.; Slack, L. H. Electrical and Optical Properties of Tin Oxide Films. *J. Am. Ceram. Soc.* **1974**, *57*, 278−279.
(54) Shanthi, E.; Dutta, V.; Banerjee, A.; Chopra, K. L. Electrical and optical properties of undoped and antimony-doped tin oxide films. *J. Appl. Phys.* **1980**, *51*, 6243−6251.
(55) Vázquez-Arreguín, R.; Aguilar-Frutis, M.; Falcony-Guajardo, C.; Castañeda-Galván, A.; Mariscal-Becerra, L.; Gallardo-Hernández, S.; Alarcón-Flores, G.; García-Rocha, M. Electrical, Optical and Structural Properties of SnO_2:Sb:F Thin Films Deposited from $Sn(acac)_2$ by Spray Pyrolysis. *ECS J. Solid State Sci. Technol.* **2016**, *5*, Q101.

https://dx.doi.org/10.1021/acsami.0c05039
ACS Appl. Mater. Interfaces 2020, 12, 25168−25177